POLYOXOMETALATES

Open Access
RESEARCH ARTICLE

Platinum-containing isopolytungstates: $[Pt_3W_{11}O_{41}]^{6.4-}$ with a linear $\{Pt_3O_{12}\}$ triad, $[Pt^{II}_2W_5O_{18}((CH_3)_2AsO_2)_2]^{4-}$ and $[Pt^{III}_2W_5O_{18}((CH_3)_2AsO_2)_4]^{4-}$ featuring direct Pt–Pt bonds

Jiayao Zhang[1], Saurav Bhattacharya[1,2], Mahmoud Elcheikh Mahmoud[1], Talha Nisar[1], Khaoula Merimi[3], Xavier López[3] ✉, Josep M. Poblet[3], Veit Wagner[1], and Ulrich Kortz[1] ✉

[1] *School of Science, Constructor University, Campus Ring 1, 28759 Bremen, Germany*
[2] *Department of Chemistry, BITS Pilani K K Birla Goa Campus, NH 17B Bypass Road, Zuarinagar, Goa – 403726, India*
[3] *Universitat Rovira i Virgili, Departament de Química Física i Inorgànica, Marcel·lí Domingo 1, 43007 Tarragona, Spain*

Cite This: *Polyoxometalates*, **2025**, *4*, 9140107

Read Online

ABSTRACT: The platinum-containing isopolytungstates $[Pt_3W_{11}O_{41}]^{6.4-}$ (**Pt_3W_{11}**), $[Pt^{II}_2W_5O_{18}((CH_3)_2AsO_2)_2]^{4-}$ (**$Pt^{II}_2W_5$**), and $[Pt^{III}_2W_5O_{18}((CH_3)_2AsO_2)_4]^{4-}$ (**$Pt^{III}_2W_5$**) were synthesized in aqueous media and characterized via single-crystal X-ray diffraction and multinuclear (^{195}Pt, ^{13}C, and ^{1}H) nuclear magnetic resonance (NMR) spectroscopy. The polyanion $[Pt_3W_{11}O_{41}]^{6.4-}$ comprises three $\{W_3O_{13}\}$ and one $\{W_2O_{10}\}$ fragments connected via three platinum atoms forming a linear $\{Pt_3O_{12}\}$ triad that exhibit direct Pt–Pt bonding (2.64–2.68 Å). The distances between the two outer Pt ions and oxygens from neighboring **Pt_3W_{11}** clusters (2.34 and 2.65 Å) are consistent with [4+1] coordination. Quantum mechanical calculations enabled the assignment of Pt oxidation states for the mixed-valence polyanion **Pt_3W_{11}**. The polyanion **$Pt^{II}_2W_5$** contains a monolacunary $\{W_5O_{18}\}^{6-}$ Lindqvist fragment coordinated via two Pt^{II} ions in square-planar geometry and two terminal dimethylarsinate groups, exhibiting a ^{195}Pt NMR signal at 610 ppm in water. By contrast, **$Pt^{III}_2W_5$** comprises two Pt^{III} ions with square-pyramidal coordination and direct Pt–Pt bonding (2.64 Å). The polyanions **Pt_3W_{11}** and **$Pt^{II}_2W_5$** were immobilized on SBA-15-apts and then tested as precatalysts for the hydrogenation of o-xylene under continuous-flow, high-pressure conditions.

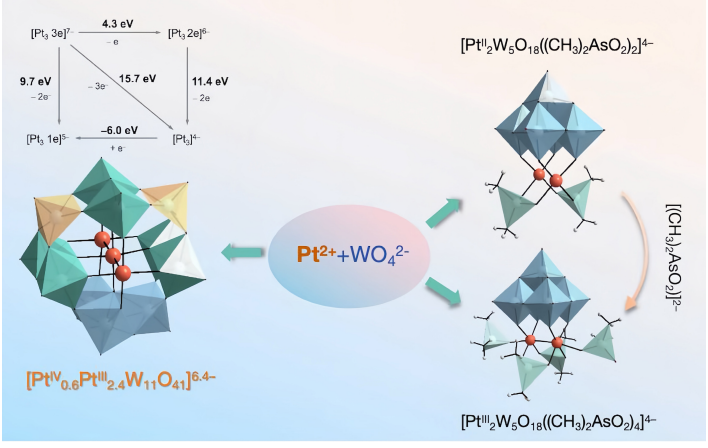

KEYWORDS: polyoxometalates, platinum, Pt–Pt bond, hydrogenation catalysis, mixed-valence compounds, quantum mechanical calculations

1 Introduction

Polyoxometalates (POMs) are discrete, soluble, polynuclear metal–oxygen cluster anions with remarkable structural and compositional versatility, accompanied by a multitude of unique physicochemical properties [1]. The subclass of noble metal-containing POMs represents a new and rapidly growing research area, mainly owing to its potential applications in catalysis and nanoscience. To date, several structural classes of noble metal-containing POMs have been synthesized (based on metals such as Pd, Pt, Ru, and Rh) [2–4]. In 2004, Wickleder and co-workers reported the first polyoxo-12-platinate(III) (POPt), $[Pt^{III}_{12}O_8(SO_4)_{12}]^{4-}$ (albeit under rather extreme experimental conditions) [5]. Our group has been developing novel synthetic approaches to construct noble metal-containing POMs with unprecedented structures for many years [6]. In this context, we pioneered the class of polyoxopalladates(II) in 2008 [7] and polyoxoaurates(III) in 2010 [8]. This novel class of polyanions is based on the condensation of oxo-bridged, square-planar MO_4 (M = Pd^{II} and Au^{III}) units, with external heterogroups capping the structure. Recently, we reported the first mixed-valent Pt^{IV}-containing hexaplatinate(II), $[Pt^{IV}Pt^{II}_6O_6(AsO_2(CH_3)_2)_6]^{2-}$ [9].

The coordination chemistry of platinum has a long history and is considered a classic field; however, surprisingly little is known about the coordination of Pt^{IV} or Pt^{II} to POMs. Well-established examples of Pt-containing POMs are sparse and are essentially restricted to a

Received: November 8, 2025; **Revised:** December 7, 2025
Accepted: December 7, 2025

✉Address correspondence to Xavier López, javier.lopez@urv.cat; Ulrich Kortz, ukortz@constructor.university

https://doi.org/10.26599/POM.2025.9140107

series of Pt^{IV}-containing Anderson–Evans-type polyanions with varying degrees of protonation [10, 11]. In 2008, Lee and Kortz prepared and structurally characterized the first platinum(IV)-containing derivative of the decavanadate ion, $[H_2Pt^{IV}V_9O_{28}]^{5-}$ [12]. In 2015, the platinum^{IV}-grafted polyoxoniobate $[Nb_6O_{19}\{Pt^{IV}(OH)_2\}]_2^{12-}$ was reported [13], followed in 2022 by the Pt^{IV}-grafted $[\{Pt^{IV}(OH)_3(H_2O)\}_6P_8W_{48}O_{184}]^{34-}$ [14]. By contrast, square-planar coordinated Pt^{II} has long remained beyond the scope of POM chemists. Only a few examples of Pt^{II}-containing POMs have been reported, such as $[Pt^{II}_2(W_5O_{18})_2]^{8-}$ [15], $[\alpha\text{-}PW_{11}O_{39}(cis\text{-}Pt^{II}(NH_3)_2)_2]^{3-}$ [16–18], *anti*- and *syn*-$[Pt^{II}_2(\alpha\text{-}PW_{11}O_{39})_2]^{10-}$ [19], and $[\alpha\text{-}PW_{11}O_{39}\{cis\text{-}Pt^{II}(Me_2ppz)\}]^{5-}$ (Me_2ppz = *N*,*N*′-dimethylpiperazine) [20]. Later studies described the electrocatalytic activity of $[Pt^{II}_2(W_5O_{18})_2]^{8-}$ in the hydrogen evolution reaction [21, 22]. To date, no complexes of tri-Pt^{II}-containing POMs have been reported. Hence, the preparation and reliable characterization of Pt-containing POMs remain a considerable challenge. In platinum(II) chemistry, it is well known that five-coordinate complexes are generally less common than four-coordinate complexes, owing to the tendency of d^8 ions to adopt a square-planar geometry. Nevertheless, five-coordinate complexes can be obtained through rational design of the coordination environment, as exemplified by cisplatin and its second-generation derivatives [23, 24]. Such complexes mainly involve halides [25, 26], pseudohalides [27, 28], hydride [29, 30], hydrocarbyl [31–34], organometal fragments [35–38], or neutral nitrogen- [39, 40] or sulfur-containing [41] ligands.

2 Experimental methods

2.1 Synthesis of $K_{2.4}Na_4[Pt_3W_{11}O_{41}]\cdot16H_2O$ (KNa–Pt_3W_{11})

K_2PtCl_4 (41.5 mg, 0.10 mmol) and Na_2WO_4 (33.0 mg, 0.10 mmol) were added to an aqueous sodium dimethylarsinate (also known as cacodylate) buffer (2 mL, 0.5 M, pH adjusted to 7 with 68% HNO_3) and stirred for 20 min at 80 °C. The initial orange-red solution first turned light brown and then deepened to a darker brown. Colorless and gray-greenish paratungstate crystals formed overnight and were filtered off after 2 days. After several days, dark red block crystals of **KNa–Pt_3W_{11}** (yield = 2.5 mg, 2% based on Pt) and additional gray-greenish crystals were obtained. The supernatant was then decanted, and the crystals were washed with 2 M sodium cacodylate buffer followed by 96% ethanol. Since **KNa–Pt_3W_{11}** crystals were almost always contaminated with crystalline gray-greenish paratungstate impurities, they were mechanically separated under a microscope, which was considerably easy owing to the color difference. Anal. Calcd (%) for **KNa–Pt_3W_{11}**: Pt 15.66, W 54.11, K 2.51, Na 2.46. Found: Pt 16.30, W 50.60, K 3.07, Na 3.79. Fourier transform infrared (FT-IR; KBr, cm^{-1}): 3,600–3,200(s) (ν(O–H) of structural H_2O), 1,622 (m) (δ(O–H) of H_2O), 1,380 (w) ($\delta_{in\text{-}plane}$(O–H)), 933 (m) (ν(W–O (terminal))), 890–768 (m) (ν(W–O (bridging))), 713 (m) (ν(Pt–O)), 497 (w) (ν(Pt–O)).

2.2 Synthesis of $Na_2K_2[Pt^{II}_2W_5O_{18}((CH_3)_2AsO_2)_2]\cdot9H_2O$ (KNa–$Pt^{II}_2W_5$) (method 1)

If the filtrate from the synthesis of **$K_{2.4}Na_4[Pt_3W_{11}O_{41}]\cdot16H_2O$** (**KNa–$Pt_3W_{11}$**) was retained and allowed to evaporate slowly, red, rod-shaped crystals of $Na_2K_2[Pt^{II}_2W_5O_{18}((CH_3)_2AsO_2)_2]\cdot9H_2O$ (**KNa–$Pt^{II}_2W_5$**) formed within 2 days, which were collected via filtration (yield = 15.0 mg, 14% based on Pt). Anal. Calcd (%) for **KNa–$Pt^{II}_2W_5$**: Pt 18.08, W 42.60, As 6.94, K 3.62, Na 2.13, C 2.23, H 1.40. Found: Pt 19.00, W 42.40, As 7.62, K 3.56, Na 2.46, C 2.77, H 1.39. FT-IR (KBr, cm^{-1}): 3,600–3,200(s) (ν(O–H) of structural H_2O), 3,026–2,853 (w) (ν(C–H) of methyl groups of cacodylate), 1,629 (m) (δ(O–H) of H_2O), 1,384 (s) (δ(C–H) methyl groups of cacodylate), 1,271 (w) ($\delta_{in\text{-}plane}$(O–H)), 925 (m) (ν(W–O (terminal))), 863 (m) (ν(W–O (bridging))), 802 (s) (ν(As–O–Pt)), 700–514 (s) (ν(Pt–O)), 406 (m) (ν(As–C)).

2.3 Synthesis of $Na_2K_2[Pt^{II}_2W_5O_{18}((CH_3)_2AsO_2)_2]\cdot9H_2O$ (KNa–$Pt^{II}_2W_5$) (method 2)

K_2PtCl_4 (16.6 mg, 0.04 mmol) and $Na_2WO_4\cdot2H_2O$ (33.0 mg, 0.10 mmol) were added to an aqueous sodium cacodylate buffer (2 mL, 1 M, pH adjusted to 7 with 68% HNO_3), stirred for 20 h at room temperature, and then stirred for additional 30 min at 80 °C. Colorless block-shaped crystals and orange, rod-shaped crystals formed within 2 weeks via slow evaporation of this solution. The orange crystals were manually selected and dried in air on filter paper (yield = 4.3 g, 10% based on Pt). FT-IR and single-crystal XRD analyses confirmed that this material is identical to that produced using method 1.

2.4 Synthesis of $Na_2K_2[Pt^{III}_2W_5O_{18}((CH_3)_2AsO_2)_4]\cdot H_2O$ (KNa–$Pt^{III}_2W_5$)

KNa–$Pt^{II}_2W_5$ (30 mg, 0.01 mmol) was added to an aqueous sodium cacodylate buffer (1.5 mL, 0.5 M, pH adjusted to 7 with 68% HNO_3) and stirred at 80 °C for 20 min. Slow evaporation of the orange solution over a week yielded orange, rod-shaped crystals of **KNa–$Pt^{II}_2W_5$** and red, cuboid-shaped crystals of **KNa–$Pt^{III}_2W_5$**. The yield of **KNa–$Pt^{III}_2W_5$** was very low, and separation of the two crystalline fractions was difficult; therefore, a bulk sample could not be collected for elemental analysis. FT-IR (KBr, cm^{-1}) on a crystal: 3,600–3,200(s) (ν(O–H) of structural H_2O), 3,026–2,936 (w) (ν(C–H) of methyl groups of cacodylate), 1,629 (m) (δ(O–H) of H_2O), 1,405 (s) (δ(C–H) of methyl groups of cacodylate), 1,274 (w) ($\delta_{in\text{-}plane}$(O–H)), 964–935 (m) (ν(W–O (terminal))), 862 (m) (ν(W–O (bridging))), 802 (s) (ν(As–O–Pt)), 700–514 (s) (ν(Pt–O)), 400 (m) (ν(As–C)).

2.5 General methods and materials

Elemental analyses were performed by the Hamburg University of Technology (TUHH, Zentrallabor Chemische Analytik, Eißendorfer Straße 38, Gebäude O, 21,073 Hamburg, Germany) and Analytische Laboratorien (Industriepark Kaiserau, Haus Heidbruch, 51,789 Lindlar, Germany). Analyses of K and Na were conducted in-house using atomic absorption (AA) spectroscopy on a Varian SpectrAA 220 AA spectrometer. The crystal water content was determined via thermogravimetric analysis (TGA) using a TA Instruments Q600 device at a heating rate of 5 °C·min^{-1} under N_2 atmosphere (20–800 °C or 500 °C). TGA of freshly prepared **KNa–Pt_3W_{11}** and **KNa–$Pt^{II}_2W_5$** showed an initial weight loss between ~ 20 and 150 °C, corresponding to lattice water (calculated: 7.5%, observed: 7.5% and 7.7%, respectively), followed by polyanion transformation/decomposition above 150 °C. FT-IR spectra (KBr pellets) were recorded on a Nicolet Avatar 370 spectrometer (4000–400 cm^{-1}). Solution ^1H and ^{13}C nuclear magnetic resonance (NMR) spectra were recorded on a JEOL ECS 400 MHz spectrometer using 5 mm tubes, with resonance frequencies of 399.78 and 100.71 MHz for ^1H and ^{13}C, respectively. ^{195}Pt NMR

spectra were recorded on a JEOL ECA 400 MHz instrument using 5 mm tubes, with a resonance frequencies of 85.94 MHz. Chemical shifts are reported relative to Na_2PtCl_6 in D_2O. All NMR measurements were performed at room temperature using H_2O/D_2O as the solvent. Catalytic hydrogenation reactions were conducted in a PID Microactivity Effi fixed-bed reactor equipped with a 9 mm SS316 stainless steel tubular reactor (internal diameter = 9.1 mm, total length = 304.8 mm). A Gilson HPLC pump was used for feed injections, and an Agilent 6,890 GC-FID with an Rtx-DHA-100 column (Restek; equivalent to DB-Petro 100 m × 250 μm × 0.5 μm, Part No. 122-10A6) was used for product analysis. The samples were injected into the gas chromatograph using a CI4W.5 switching valve (0.5 μL injection volume) from VICI.

X-ray crystallography. Data for **KNa–Pt_3W_{11}**, **KNa–$Pt^{II}_2W_5$**, and **KNa–$Pt^{III}_2W_5$** were collected at 100 K on a Rigaku XtaLAB Synergy, Dualflex, HyPix single-crystal diffractometer equipped with kappa geometry (graphite monochromator, $\lambda_{Mo\ K\alpha}$ = 0.71073 Å) using CrysAlis^{Pro} software package [42]. The crystal was mounted in Hampton cryoloop with paratone-N oil. Multi-scan absorption corrections were applied using the ABSPACK [43] and SADABS program [44]. The structures were solved using direct methods aided by successive difference Fourier maps and refined against all data using SHELXL-2014 [45]. The H atoms of the cacodylate methyl groups were placed in calculated positions and refined using a riding model, while the remaining non-hydrogen atoms were refined with anisotropic displacement parameters. Refinements were conducted via full-matrix least squares against $|F|$ using all data. Images of the crystal structures were generated using Diamond, version 3.2 (Crystal Impact GbR). Some lattice water molecules were highly disordered, and the corresponding disagreeable reflections were removed using the SQUEEZE command in PLATON [46]. Crystallographic data for **KNa–Pt_3W_{11}**, **KNa–$Pt^{II}_2W_5$**, and **KNa–$Pt^{III}_2W_5$** are summarized in Table 1. CIF files are available free of charge from The Cambridge Crystallographic Data Centre (CSD 2414132, CCDC 2414130, and CCDC 2414131).

2.6 Computations

All calculations were conducted using density functional theory (DFT) with the Gaussian16 software [47–49]. Gaussian-type

Table 1 Single crystal data and structure refinement parameters for **KNa–Pt_3W_{11}**, **KNa–$Pt^{II}_2W_5$**, and **KNa–$Pt^{III}_2W_5$**

Compound	**KNa–Pt_3W_{11}**	**KNa–$Pt^{II}_2W_5$**	**KNa–$Pt^{III}_2W_5$**
Empirical formula	$K_{2.4}Na_4Pt_3W_{11}O_{57}H_{32}$[a]	$K_2Na_2Pt_2W_5As_2O_{31}C_4H_{30}$[a]	$K_2Na_2Pt_2W_5As_4O_{38}C_8H_{24}$
fw (g·mol^{-1})	3737.54[a]	2157.64[a]	2445.56
Crystal system	Triclinic	Monoclinic	Monoclinic
Space group	$P\bar{1}$	$P2/n$	$C2/c$
a (Å)	12.6266(3)	16.9228(3)	17.2840(3)
b (Å)	13.6378(4)	11.8389(2)	11.6921(2)
c (Å)	17.5633(4)	17.8814(3)	22.3889(4)
α (°)	82.104(2)	90	90
β (°)	82.452(2)	93.2993(17)	93.0538(14)
γ (°)	64.519(3)	90	90
V (Å^3)	2695.47(13)	3576.56(12)	4518.08(13)
Z	1	4	4
Dc (g·cm^{-3})	4.459	4.003	3.595
Abs coeff. (mm^{-1})	31.401	25.999	22.056
F(000)	3102	3776	4344
θ range for data collection (°)	2.349 to 25.026	2.411 to 25.025	2.318 to 31.677
Completeness to θ_{max}	99.9%	99.9%	89.2%
Index ranges	$-15 \le h \le 15$ $-16 \le k \le 16$ $-20 \le l \le 20$	$-19 \le h \le 20$ $-14 \le k \le 14$ $-21 \le l \le 21$	$-24 \le h \le 24$ $-16 \le k \le 16$ $-32 \le l \le 33$
Reflns collected	31,292	25,593	57,273
Indep reflns	9501	6320	6818
R(int)	0.0616	0.0463	0.0383
Abs corn	Semi-empirical from equivalents	Semi-empirical from equivalents	Semi-empirical from equivalents
Data/restaints/param	9501/30/658	6320/0/443	6818/144/290
GOF on F^2	1.039	1.064	1.099
R_1[b], wR_2[c] [$I > 2\sigma(I)$]	0.0487, 0.1304	0.0300, 0.0726	0.0295, 0.063
R_1[b], wR_2[c] (all data)	0.0595, 0.1384	0.0336, 0.0739	0.0361, 0.0651
Largest diff peak and hole (e·Å^{-3})	4.389 and −3.800	1.922 and −2.000	7.618 and −2.147

[a]The entries represent the formula units and weights obtained from a combination of all experimental techniques, mainly elemental analysis and XPS, reflecting the true composition of the bulk material.
[b]$R_1 = \Sigma||F_o| - |F_c||/\Sigma|F_o|$.
[c]$wR_2 = [\Sigma w(F_o^2 - F_c^2)^2/\Sigma w(F_o^2)^2]^{1/2}$.

functions were employed to represent the atomic basis sets. For oxygen (O) atoms, the 6-31G(d,p) basis set was utilized, while tungsten and platinum atoms were described using the Los Alamos National Laboratory pseudopotential with the standard double-zeta LANL2DZ basis set [50]. The LANL2DZ(f) basis set includes an effective core potential that accounts for relativistic effects on the internal electron shells. Geometry optimizations and electronic state energy calculations were performed with the hybrid PBE0 functional [51]. Empirical dispersion corrections were included using Grimme's Dispersion 3 with Becke–Johnson damping (GD3BJ) [52]. Solvation effects in aqueous solution were modeled using the polarizable continuum model (PCM) [53, 54]. Additionally, the explicit inclusion of crystal cations ("PCM + cations" setup) was considered for comparison, as discussed at the end of the Results section.

3 Results and discussion

3.1 Synthesis and characterization of the tri-Pt-containing isopoly-11-tungstate $[Pt_3W_{11}O_{41}]^{6.4-}$

We synthesized the tri-Pt-containing isopolytungstate $[Pt_3W_{11}O_{41}]^{6.4-}$ (**Pt_3W_{11}**) via the reaction of K_2PtCl_4 with $Na_2WO_4{\cdot}2H_2O$ in aqueous medium, during which the solution color changed rapidly overnight (from the initial orange-red to brown, becoming increasingly intense). Slow evaporation of the solution yielded gray-greenish and dark red, block-shaped crystals (Fig. S1 in the Electronic Supplementary Material (ESM)), which were separated via fractional crystallization. The dark red crystals, comprising **Pt_3W_{11}**, were isolated as a mixed potassium–sodium salt, $K_{2.4}Na_4[Pt^{IV}_{0.6}Pt^{III}_{2.4}W_{11}O_{41}]{\cdot}16H_2O$ (**KNa–Pt_3W_{11}**). The mixed potassium–sodium salt of polyanion **Pt_3W_{11}** crystallized in a triclinic lattice with space group $P\bar{1}$ (single-crystal data are provided in Table 1). This unprecedented polyanion features a central, linear Pt_3O_{12} platinum–oxo unit encapsulated by an unusual $W_{11}O_{41}$ tungsten–oxo ring, which comprises a corner-sharing W_3O_{13} group (formed via three edge-sharing WO_6 octahedra), two corner-sharing WO_5 groups, and three corner-sharing W_2O_{10} groups. The three W_2O_{10} groups and two WO_5 square pyramids alternate along the ring (Fig. 1). The linear Pt_3O_{12} unit is positioned along the central axis of the $W_{11}O_{41}$ ring, suggesting that the former may act as a template, resulting in a structure with C_s symmetry. The central Pt atom is six-coordinated, with four oxygen atoms arranged in a square-planar geometry (originating from three dinuclear and one trinuclear tungsten–oxo units) and a metal–metal bond with the two neighboring Pt atoms. The two outer Pt atoms are five-coordinated, each bonded to four oxygen atoms (from three dinuclear and one trinuclear tungsten–oxo units) and forming a metal–metal bond with the central Pt atom. The Pt–Pt distances in **Pt_3W_{11}** are 2.636(2) and 2.674(4) Å, suggesting metal–metal bonding among the three Pt atoms (see Tables S1–S4 and S6 in the ESM for selected bond lengths) [55]. The Pt···O distances in $[Pt_3W_{11}O_{41}]^{6.4-}$ range between 2.368(1) and 2.630(1) Å (Table S6 in the ESM), and the relevant bond angles are provided in Table S7 in the ESM. In the solid state, neighboring **Pt_3W_{11}** ions interact via Pt···O contacts in a [4+1] coordination mode (four planar Pt–O bonds and one axial interaction), resulting in a zig-zag chain (Fig. S2 in the ESM). The exact assignment of oxidation states for the three platinum atoms in **Pt_3W_{11}** is complex; hence, we performed X-ray photoelectron spectroscopy (XPS) combined with quantum mechanical calculations.

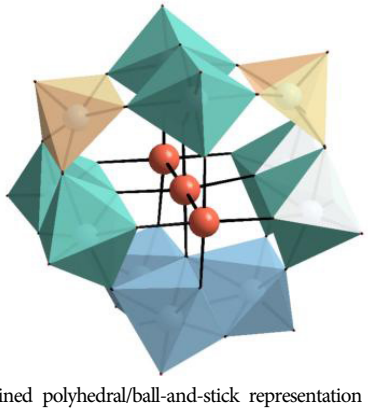

Figure 1 Combined polyhedral/ball-and-stick representation of $[Pt_3W_{11}O_{41}]^{6.4-}$ (**Pt_3W_{11}**). Pt red, WO_6 blue and green octahedra, and WO_5 orange square-pyramids.

3.2 XPS and quantum mechanical calculations

To determine the oxidation states of the three Pt atoms in **Pt_3W_{11}**, we performed XPS measurements on **KNa–Pt_3W_{11}** after grinding the crystalline sample to ensure a homogeneous surface composition. These measurements were supplemented with quantum mechanical analyses to univocally characterize the system and explain its behavior. The XPS analysis on **KNa–Pt_3W_{11}** revealed an atomic Pt^{IV}:Pt^{III} ratio of 1:4 (Fig. 2). This relative abundance can be formally expressed in terms of a mixed-valence scenario $[Pt^{IV}_{0.6}Pt^{III}_{2.4}W_{11}O_{41}]^{6.4-}$, although for an individual polyanion, it must be achieved as a combination of $Pt_3W_{11}O_{41}$ units comprising an integer number of Pt ions in a given oxidation state. In principle, several arrangements satisfy the 1:4 ratio—for example, a mixture of species such as 1 $[Pt^{IV}{}_3W_{11}O_{41}]^{4-}$:4 $[Pt^{III}{}_3W_{11}O_{41}\ 3e]^{7-}$. In this notation, *x*e denotes the number of extra electrons relative to the fully oxidized all-Pt^{IV} species, $[Pt^{IV}{}_3W_{11}O_{41}]^{4-}$. Other combinations of oxidation states for the polyanion are also possible. To explore this, we conducted a quantum mechanical study on the series of $[Pt_3W_{11}O_{41}\ xe]^{n-}$ species with x = 0–3, which can give rise to mixtures of Pt oxidation states within a single polyanion. This analysis provides additional evidence of the most probable combination of $[Pt_3W_{11}O_{41}\ xe]^{n-}$ units in the crystal. For simplicity, the shortened nomenclature $[Pt_3\ xe]^{n-}$ is used in the

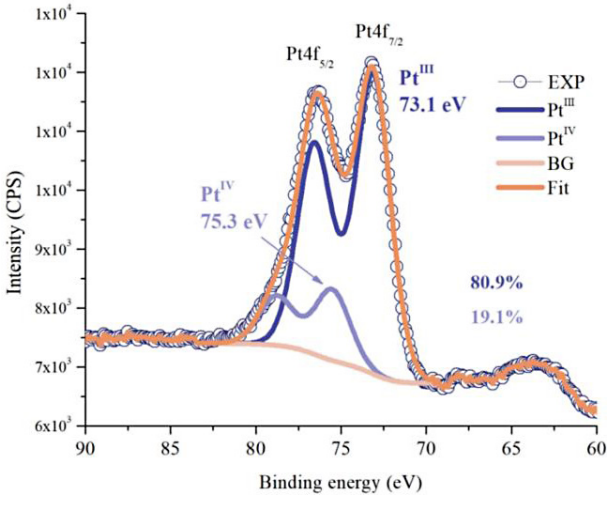

Figure 2 X-ray photoelectron spectrum of **KNa-Pt_3W_{11}** and fits for the Pt $4f_{7/2}$ and $4f_{5/2}$ doublet.

following discussion.

To determine the most probable composition of the **KNa–Pt_3W_{11}** crystal structure, i.e., which $[Pt_3\ xe]^{n-}$ units are present and their abundances, the computational analysis focused on the electronic structures and molecular energies of several $[Pt_3W_{11}O_{41}]^{n-}$ variants, including possible combinations of Pt oxidation states within the same Pt_3 unit. For each species considered that could potentially satisfy the experimentally observed Pt^{IV}:Pt^{III} ratio in the crystal, different spin states were contemplated. The results are summarized in Table S2 in the ESM.

3.2.1 *Pt_3 with a varying number of electrons*

In this section, we refer to calculations performed using the "PCM" setup—that is, including environmental effects via the PCM method (see computational details) but not explicitly including the cations of the crystal, to generate the electronic structure of the POMs.

Starting with the $[Pt_3]^{4-}$ and $[Pt_3\ 3e]^{7-}$ systems, we identified the quintet and quartet spin multiplicities, respectively, as the most stable (Fig. S3 in the ESM), as shown in Table S2 in the ESM, with consistent $\langle S^2 \rangle$ values. For the $[Pt_3]^{4-}$ case, we found a nearly degenerate triplet with a very similar electronic distribution (corresponding to a flip of a single Pt unpaired electron). Thus, as suggested above, one possible combination to meet the experimental 1:4 Pt^{IV}:Pt^{III} ratio is one $[Pt_3]^{4-}$ unit together with four $[Pt_3\ 3e]^{7-}$ units.

Calculations on the mixed-valence $[Pt_3\ 2e]^{6-}$ structure yield three quasi-degenerate spin arrangements: one singlet and two triplets, in which the valence Pt 5d electrons are distributed equally along the Pt_3 motif. The singlet state represents an open-shell (↑–↓) broken-symmetry solution. Its $\langle S^2 \rangle$ value of 1.02 denotes large spin contamination from higher multiplicities, notably the aforementioned triplets.

The $[Pt_3\ 2e]^{6-}$ structure (i.e., formally $Pt^{IV}Pt^{III}_2$), combined with $[Pt_3\ 3e]^{7-}$ units in a 3:2 ratio, also reproduces the experimentally observed Pt^{IV}:Pt^{III} ratio of 1:4. This combination is 62.7 kcal·mol^{-1} more stable than the 1 $[Pt_3]^{4-}$:4 $[Pt_3\ 3e]^{7-}$ arrangement, a considerable energy difference revealing that the crystal very likely contains mixed-valence Pt_3 units. This finding can be rationalized via a criterion of maximal similarity of molecular charges among the various POM moieties in the crystal. In other words, this result highlights the instability of having in the same crystal molecular units with very dissimilar charges, such as all-Pt^{IV} units (with charge −4) and all-Pt^{III} units (with charge −7). The energies associated with electron gain or removal, approximated as the electronic energy differences between Pt_3 units with different electron counts, are shown in Scheme 1.

We observe that the energy required to remove one electron from $[Pt_3\ 3e]^{7-}$ is 4.3 eV, which is significantly lower than the 11.4 eV required to remove the two remaining electrons from $[Pt_3\ 2e]^{6-}$ to reach the fully oxidized form $[Pt_3]^{4-}$. These values further support the likelihood of the 3 $[Pt_3\ 2e]^{6-}$:2 $[Pt_3\ 3e]^{7-}$ combination.

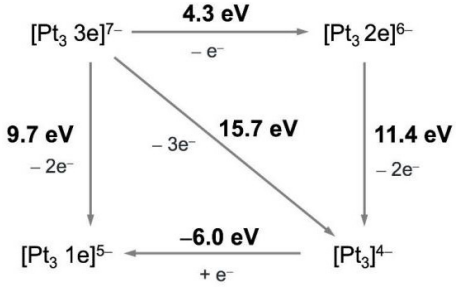

Scheme 1 Energies associated to electron gain/loss for the Pt_3 system.

We also analyzed the molecular orbital sequence for the different systems, as shown in Fig. 3, revealing differences in stability. Given the open-shell nature of the Pt_3 motif, the α and β orbital sets obtained from DFT calculations are represented separately. For α/β-compensated electronic configurations (such as $[Pt_3\ 2e]^{6-}$), both sets are equivalent. However, an excess of α electrons (as in $[Pt_3\ 3e]^{7-}$) leads to considerable differences in the frontier orbital region. These differences can impact some properties of the system, including reactivity and magnetic behavior. When comparing $[Pt_3\ 3e]^{7-}$ and $[Pt_3]^{4-}$, the highest occupied orbital (HOMO) of the former is only 0.1 eV lower than the lowest unoccupied orbital (LUMO) of the latter, indicating marginal (or no) stability and suggesting that one or more electrons would immediately transfer from the electron-rich $[Pt_3\ 3e]^{7-}$ species to the highly oxidizing $[Pt_3]^{4-}$, thereby compensating their charges. Conversely, the energy difference between the LUMO of $[Pt_3\ 2e]^{6-}$ and the HOMO of $[Pt_3\ 3e]^{7-}$ is much larger (ΔE = 1.1 eV), indicating notable stability of the ensemble for this combination.

Notably, the one-electron reduced species $[Pt_3\ 1e]^{5-}$ (Fig. 3) was also considered in the present computational study. Calculations show that the most stable spin state for this species corresponds to a quartet (Table S2 in the ESM).

Nevertheless, if we do not restrict ourselves to considering only two types of Pt_3 moieties, another possibility emerges: combining the $[Pt_3\ 3e]^{7-}$ form with the mixed-valence variants $[Pt_3\ 2e]^{6-}$ and $[Pt_3\ 1e]^{5-}$ in an overall ratio 3:1:1. When comparing the stability of this 3:1:1 combination with that of 3 $[Pt_3\ 2e]^{6-}$:2 $[Pt_3\ 3e]^{7-}$, the latter remains the most stable.

Concerning structural features, we compared the experimentally determined and the DFT-calculated Pt···Pt and Pt–O distances (Table S1 in the ESM). The $[Pt_3]^{4-}$ system presents the poorest agreement with the experimental data, whereas the mixed-valence $[Pt_3W_{11}O_{41}\ 2e]^{6-}$ system exhibits the best match.

Moreover, a Bader charge analysis was performed on the calculated electron density for all systems [56]. In general, although we formally refer to Pt^{III} and Pt^{IV}, the complexity of the system causes the valence electrons of Pt to be delocalized over the Pt_3 motif and their neighboring oxo ligands, which can be classified as class III in the Robin–Day scheme of mixed-valence compounds. To support this, we computed the hypothetical process of electron subtraction $[Pt_3\ 3e]^{7-} \rightarrow [Pt_3\ 2e]^{6-} + e^-$, revealing that the electron is distributed equally among the three Pt atoms, resulting in a balanced electron loss of ~ 0.2 e per PtO_4 group (Table S3 in the ESM), with the remainder drawn from the rest of the polyanion. This observation aligns with the shape of the donating HOMO of $[Pt_3\ 3e]^{7-}$ (Fig. S4 in the ESM), which shows similar contributions from all Pt atoms. By contrast, further oxidation of $[Pt_3\ 2e]^{6-}$ to generate $[Pt_3\ 1e]^{5-}$ removes the electron mostly from the central Pt (~ 0.5 e). These results suggest that the platinum atoms in **Pt_3W_{11}** cannot always be assigned integer oxidation states.

The same Bader analysis provides information about the nature of the Pt–Pt interactions. A search for the critical points in all Pt_3 systems across different spin multiplicities allowed us to systematically identify two bond critical points (BCPs) located within the Pt–Pt–Pt moiety. The corresponding electron density (ρ) and density Laplacian ($\nabla^2\rho$) values are shown in Table S4 in the ESM and compared with BCP parameters for selected Pt–O bonds in the same systems. The obtained values are r(Pt–Pt BCP) =

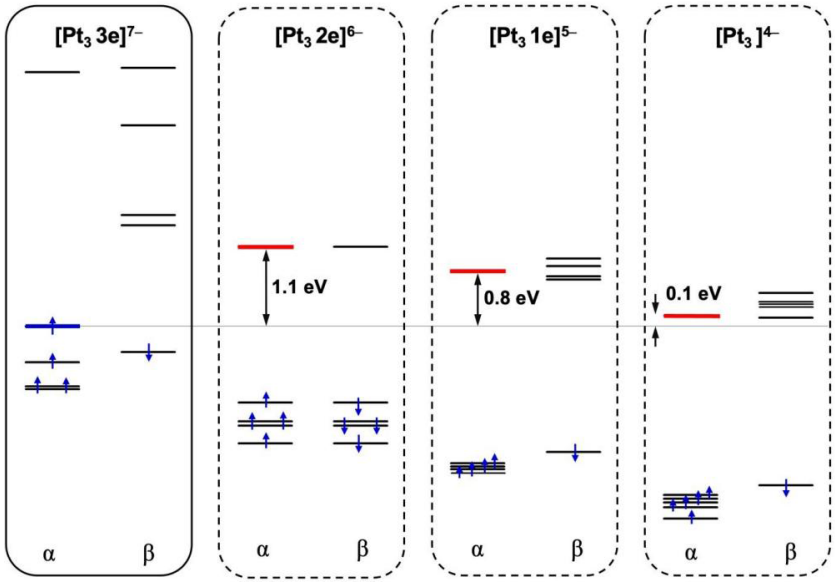

Figure 3 Molecular orbitals sequence (α and β sets) resulting from the quantum mechanical analysis on the $[Pt_3\ xe]$ series. The energy gaps between the HOMO of $[Pt_3\ 3e]^{7-}$ (horizontal line) and the LUMOs of the less electron-rich forms ($x = 2$, 1 and 0) are shown.

0.034–0.064 e·bohr^{-3} and $\nabla^2\rho$(Pt–Pt BCP) = 0.071–0.115 e·bohr^{-5}, with variations stemming from differences in Pt oxidation states, interatomic distances, and electron multiplicities. These results align with BCP values reported for heavy open-shell atoms, confirming the presence of Pt–Pt bonds in all cases. Previous studies on similar moieties have shown comparable features [57, 58]. To complement these findings, we calculated the multicenter bond index (MCBI) based on the spin- pure triplet state of the $[Pt_3\ 2e]^{6-}$ cluster, obtaining a value of MCBI = 1.95, consistent with a 2-electron-3-center bond. Additional pairwise bond indices were also evaluated; further details are provided in Table S5 in the ESM.

Additional analysis of the molecular orbitals, shown in detail in Fig. S4 in the ESM, further clarifies some geometrical trends, such as the $[Pt_3\ 2e]^{6-}$ system featuring shorter Pt–Pt distances than its one-electron reduced partner, $[Pt_3\ 3e]^{7-}$.

3.2.2 Incorporation of explicit counterions

The previous computational results were obtained including the effect of the crystal environment in a simplified manner; that is, the positions and nature of the cations surrounding a given polyanion were not explicitly considered (Table S2 in the ESM, "PCM" columns). In this setup, the polyanion is treated as being embedded in a continuum dielectric material with no explicit cations. For comparison, additional computations were performed by extending the model with the cations nearest to the polyanion, placed at their crystallographic positions (Table S2 in the ESM, "PCM + cations" columns). In general, the results obtained with either setup show good agreement, with the lowest-energy state of the polyanion in its different reduction states remaining the same. For the $[Pt_3\ 2e]^{6-}$ system, although the most stable state does not exactly coincide between the two setups, the three lowest-energy states lie within a narrow energy range, indicating that any of these states could dominate the electronic structure at room temperature. The consistency in energy ordering between the two setups (Table S1 in the ESM) suggests that crystal packing has a limited effect on the electronic structure of the polyanion.

The computational results strongly suggest that the coexistence of the $[Pt_3W_{11}O_{41}]^{4-}$ and $[Pt_3W_{11}O_{41}\ 3e]^{7-}$ species in the crystal is unlikely. A more chemically plausible and stable combination involves polyanions such as $[Pt_3\ 2e]^{6-}$ and $[Pt_3\ 3e]^{7-}$ in a 3:2 ratio, as supported by their respective HOMO and LUMO energies. In general, the oxidation state of each Pt center in $\mathbf{Pt_3W_{11}}$ cannot be strictly assigned as +3 or +4.

3.3 Synthesis and characterization of the di-Pt-containing isopoly-5-tungstates $[Pt^{II}_2W_5O_{18}((CH_3)_2AsO_2)_2]^{4-}$ and $[Pt^{III}_2W_5O_{18}((CH_3)_2AsO_2)_4]^{4-}$

When the filtrate was retained after the separation of $\mathbf{Pt_3W_{11}}$ crystals, red rod-shaped crystals formed within 2 days. These correspond to a di-Pt^{II}-containing isopoly-5-tungstate capped by two dimethylarsinate (cacodylate) groups, $[Pt^{II}_2W_5O_{18}((CH_3)_2AsO_2)_2]^{4-}$ ($\mathbf{Pt^{II}_2W_5}$; Fig. 4). This polyanion was isolated as a hydrated mixed potassium–sodium salt, $K_2Na_2[Pt^{II}_2W_5O_{18}((CH_3)_2AsO_2)_2]\cdot 9H_2O$ (**KNa–$Pt^{II}_2W_5$**; Table 1). The $\mathbf{Pt^{II}_2W_5}$ polyanion comprises a monovacant W_5 Lindqvist fragment with two Pt^{II} ions coordinated in a square-planar geometry, each bridged via dimethylarsinate groups (Fig. 4). The Pt–O distances are in the range of 1.970(7)–2.044(7) Å, and the Pt···Pt distance is 2.983(8) Å, indicating the absence of metal–metal bonding, although it is 0.15 Å shorter than in the sandwich-type $[Pt^{II}_2(W_5O_{18})_2]^{8-}$ [11]. The

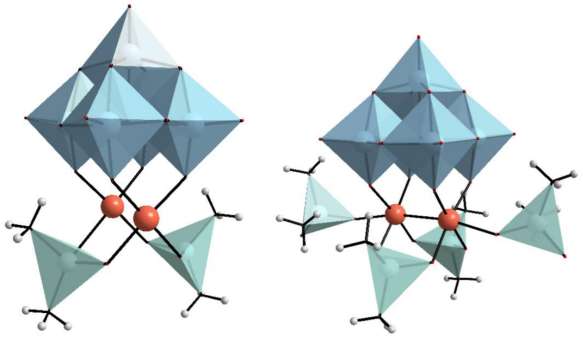

Figure 4 Combined polyhedral/ball-and-stick representation of $\mathbf{Pt^{II}_2W_5}$ (left) and $\mathbf{Pt^{III}_2W_5}$ (right). Pt red, $\{WO_6\}$ blue octahedra, $\{(CH_3)_2AsO_2\}$ green tetrahedra.

O–Pt–O angles in $\mathbf{Pt^{II}_2W_5}$ are 86.7(3)°–91.8(3)° for *cis* angles and 173.0(3)°–176.8(3)° for *trans* angles (Table S8 in the ESM).

The Pt^{III}-containing analog, $[Pt^{III}_2W_5O_{18}((CH_3)_2AsO_2)_4]^{4-}$ ($\mathbf{Pt^{III}_2W_5}$), was synthesized via the reaction of $\mathbf{KNa\text{-}Pt^{II}_2W_5}$ with sodium dimethylarsinate $Na(CH_3)_2AsO_2$ in aqueous medium. The $\mathbf{Pt^{III}_2W_5}$ polyanion comprises two six-coordinated Pt^{III} ions that are directly metal–metal bonded, each carrying a terminal dimethylarsinate ligand (Fig. 4). This high-valent polyanion crystallized as a hydrated mixed potassium–sodium salt, $K_2Na_2[Pt^{III}_2W_5O_{18}((CH_3)_2AsO_2)_4]\cdot H_2O$ ($\mathbf{KNa\text{–}Pt^{III}_2W_5}$). The Pt···Pt distance in $\mathbf{Pt^{III}_2W_5}$ is 2.639(2) Å, indicating the presence of a metal–metal bond. This suggests that $\mathbf{Pt^{III}_2W_5}$ is likely generated via air oxidation of $\mathbf{Pt^{II}_2W_5}$, followed by coordination of two extra dimethylarsinate ligands to stabilize the higher oxidation state of Pt. Similar coordination geometries with metal–metal bonds are observed in the $\{Rh^{III}_2\}$ dimer (2.52(2) Å) and the $\{Pt^{III}_2\}$ dimer (2.46 Å) also [59–63].

The Pt–O bond lengths are 1.990(12)–2.144(12) Å, with the longest bond distance corresponding to the terminal dimethylarsinate ligand. The O–Pt–O angles in $\mathbf{Pt^{III}_2W_5}$ are 79.8(2)°–91.7(2)° for the angles reflecting bonding to the $\{W_5O_{18}\}$ moiety, and 171.51(2)°–172.51(2)° for the more linear angles, which are slightly smaller than in $\mathbf{Pt^{II}_2W_5}$ (Tables S8 and S9 in the ESM). The O–Pt–Pt–O angles are not colinear, measuring 169.6(1)° at the Pt atoms, owing to the steric hindrance from the tungsten–oxo unit, which causes the terminal dimethylarsinate ligands to bend slightly outward. In the solid state, the discrete polyanions are surrounded by K^+ and Na^+ countercations, which coordinate to both oxygen atoms of the dimethylarsinate ligands and the water molecules of hydration.

To complement our solid-state studies of $\mathbf{Pt^{II}_2W_5}$, we performed ^1H, ^{13}C, and ^{195}Pt NMR spectroscopy on $\mathbf{KNa\text{–}Pt^{II}_2W_5}$ dissolved in water. The ^1H NMR spectrum of the reference compound, sodium dimethylarsinate (Na-cac), in water exhibits a singlet at 1.4 ppm and the solvent peak at 4.7 ppm. In the ^1H NMR spectrum of $\mathbf{Pt^{II}_2W_5}$, two peaks are observed at 1.8 and 1.6 ppm, corresponding to the two structurally and hence magnetically inequivalent methyl groups on each dimethylarsinate ligand (Fig. 5). The ^1H NMR spectrum of $\mathbf{Pt^{II}_2W_5}$ remained unchanged over 5 days, indicating high solution stability of this polyanion. The ^{13}C NMR spectrum of $\mathbf{Pt^{II}_2W_5}$ exhibits the expected two peaks at 19.4 and 16.6 ppm (Fig. 5), while the ^{13}C NMR spectrum of the reference Na-cac in water shows a singlet at 17.4 ppm.

We also performed ^{195}Pt NMR spectroscopy on $\mathbf{KNa\text{–}Pt^{II}_2W_5}$ dissolved in water and observed the expected singlet at 610 ppm (Fig. 6). The corresponding ^{195}Pt NMR signal for the precursor K_2PtCl_4 appeared significantly more upfield at −1,616 ppm. To date, successful ^{195}Pt NMR studies on POMs are rather rare owing to the very large chemical shift anisotropy of ^{195}Pt [64]. A positive example is $[H_2Pt^{IV}V_9O_{28}]^{5-}$ reported by Lee and Kortz in 2008, which exhibit a clean singlet at 3,832 ppm [12]. In 2015, the ^{195}Pt NMR spectra of the above-mentioned Pt^{IV}-containing polyoxoniobates exhibited singlets at 3,189 ppm for $[Nb_6O_{19}\{Pt(OH)_2\}]_2^{12-}$ and 3,422 ppm for $[Pt(Nb_6O_{19})_2]^{12-}$ [13, 14]. In 2014, Klemperer's $[H_2SiPt^{IV}W_{11}O_{40}]^{4-}$ showed a ^{195}Pt signal at 3,666 ppm in acetonitrile [65]. In 1996, Kuznetsova observed a ^{195}Pt NMR signal at −1,179 ppm for an aqueous reaction of $[PW_{11}O_{39}]^{7-}$ with $[PtCl_4]^{2-}$ [66]. In 2011, Lefebvre reported a ^{195}Pt NMR chemical shift of −3,962 ppm for a DMSO solution of the $[SiW_{12}O_{40}]^{4-}$ Keggin ion with $[Pt^{II}(CH_3)(COD)]^+$ moieties grafted on its surface [67]. Then, Kato observed broad ^{195}Pt NMR signals for Pt^{II}-grafted $[PW_{11}O_{39}(cis\text{-}Pt(NH_3)_2)_2]^{3-}$ [16-18] and $[PW_{11}O_{39}\{cis\text{-}Pt^{II}(Me_2ppz)\}]^{5-}$ (Me_2ppz = *N*,*N*′-dimethylpiperazine) [20]. In 2016, Dalal and Kortz reported the feasibility of applying high-resolution solid-state ^{195}Pt MAS NMR spectroscopy for several Pt^{IV}-containing polyoxotungstates and a polyoxovanadate [68].

Hydrogenation catalysis. The two structurally distinct platinum-substituted polyanions, $\mathbf{Pt_3W_{11}}$ and $\mathbf{Pt^{II}_2W_5}$, were immobilized on SBA-15 functionalized with aminopropyltriethoxysilane (**apts**) and then evaluated for their catalytic performance in the hydrogenation of *o*-xylene to *cis*- and *trans*-1,2-dimethylcyclohexane (**1,2-DMCH**) under high-pressure hydrogen using an EFFI reactor coupled to an online gas chromatograph. For all catalytic runs, 350 mg of immobilized POM on SBA-15-apts was used. To ensure proper heat distribution and flow dynamics, 11 g of silicon carbide (SiC, 120 grit) was first added to the bottom of the reactor tube. This was followed by the 350 mg of calcined 1% Pt-POM-SBA-15-apts, placed as a fixed-bed layer. An additional ~ 3 g of SiC was then added on top to secure the catalyst bed and maintain uniform gas flow. The reactor was packed in such a way that the thermocouple tip was positioned precisely within the catalyst bed, ensuring accurate temperature monitoring during the reaction. Notably, during calcination and hydrogenation, the initial POMs are fully reduced, producing metallic Pt(0) nanoparticles, which serve as the true catalyst species. The hydrogenation activity of both supported POMs increased steadily with temperature (150–310 °C), with $\mathbf{Pt_3W_{11}}$**-SBA-15-apts** showing a maximum conversion of 85% at 310 °C, compared to 78% for $\mathbf{Pt^{II}_2W_5}$**-SBA-15-apts** (Fig. 7). This

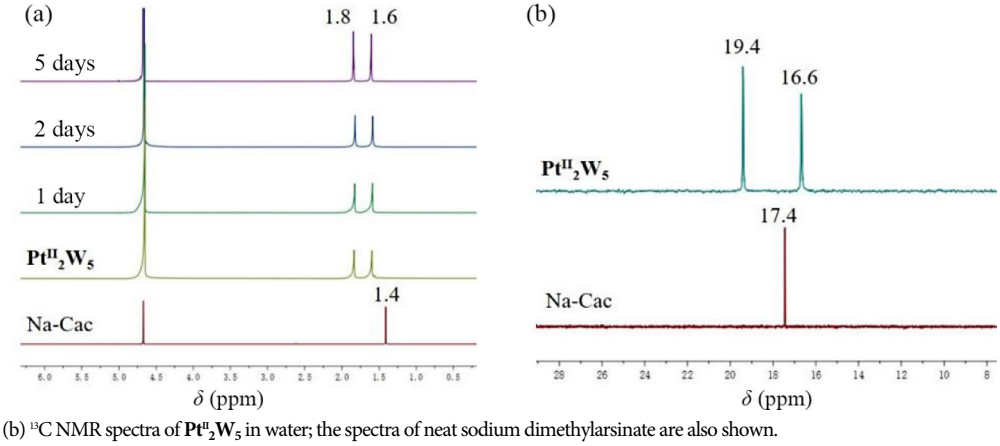

Figure 5 (a) ^1H and (b) ^{13}C NMR spectra of $\mathbf{Pt^{II}_2W_5}$ in water; the spectra of neat sodium dimethylarsinate are also shown.

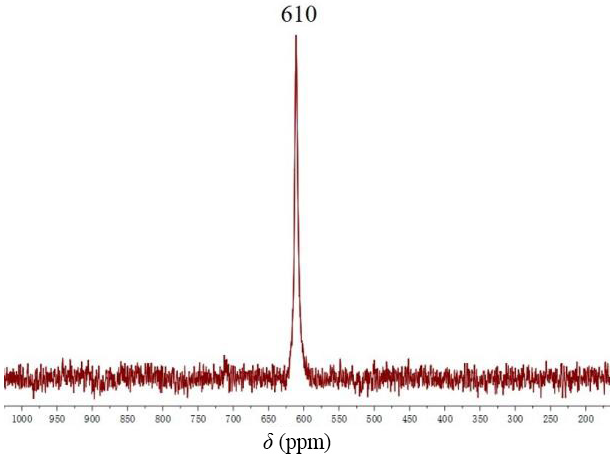

Figure 6 Room temperature ^{195}Pt NMR spectrum of $\mathbf{Pt^{II}_2W_5}$ in water.

difference is primarily attributable to the structural differences of the polyanions: $\mathbf{Pt_3W_{11}}$ comprises a compact, fully inorganic trinuclear platinum cluster stabilized within a tungsten–oxo shell, resulting in higher platinum density and more thermally stable active sites post-calcination. By contrast, $\mathbf{Pt^{II}_2W_5}$ comprises two platinum ions sandwiched by two diorganoarsinate moieties and a pentatungsten–oxo unit, which may reduce framework integrity at elevated temperatures. The *cis*/*trans* product distribution across temperatures followed a classic kinetic-to-thermodynamic transition (Fig. 7). At low temperatures (150–230 °C), ***cis*-1,2-DMCH** was favored owing to rapid formation and surface binding preferences. At temperatures above 270 °C, the thermodynamically stable ***trans*-1,2-DMCH** dominated, reflecting increased energy input and surface equilibration.

A fixed-temperature flow-rate study at 310 °C further reinforced the importance of residence time. As the *o*-xylene flow increased from 0.05 to 0.40 mL·min^{-1}, the conversion dropped substantially for both supported POMs, accompanied by corresponding changes in product distribution (Fig. 8). These results highlight the critical role of contact time in achieving deep hydrogenation of aromatic rings.Interestingly, both supported POMs demonstrated excellent reusability, maintaining stable conversion and selectivity profiles over five consecutive cycles at 310°C without pronounced deactivation or structural breakdown (Fig. S8 in the ESM). This thermal and operational robustness is attributable to covalent anchoring on SBA-15-apts and the stability of the active catalyst formed under hydrogen-rich conditions. As controls, SiC and bare SBA-15-apts supports were tested under identical reaction conditions, and no measurable conversion of *o*-xylene was observed, confirming the essential role of the two Pt-POMs in catalytic activity. Compared to the supported $[Pt_3S_2(SO_3)_6]^{10-}$

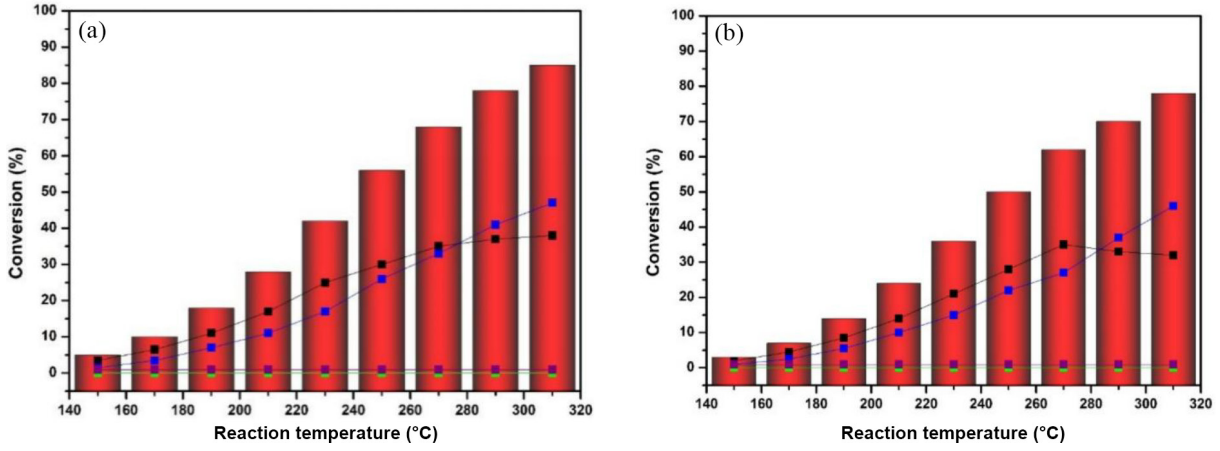

Figure 7 Hydroconversion of *o*-xylene to **1,2-DMCH** at various reaction temperatures using (a) $\mathbf{Pt_3W_{11}}$**-SBA-15-apts** and (b) $\mathbf{Pt^{II}_2W_5}$**-SBA-15-apts** as the precatalyst. Conditions: 28 bar H_2, flow rate 0.05 mL·min^{-1}. The curves represent the percentage of ***cis*-1,2-DMCH** (black) and ***trans*-1,2-DMCH** (blue) isomers in the product. Neat SBA-15-apts (purple) and SiC (green) are shown for comparison.

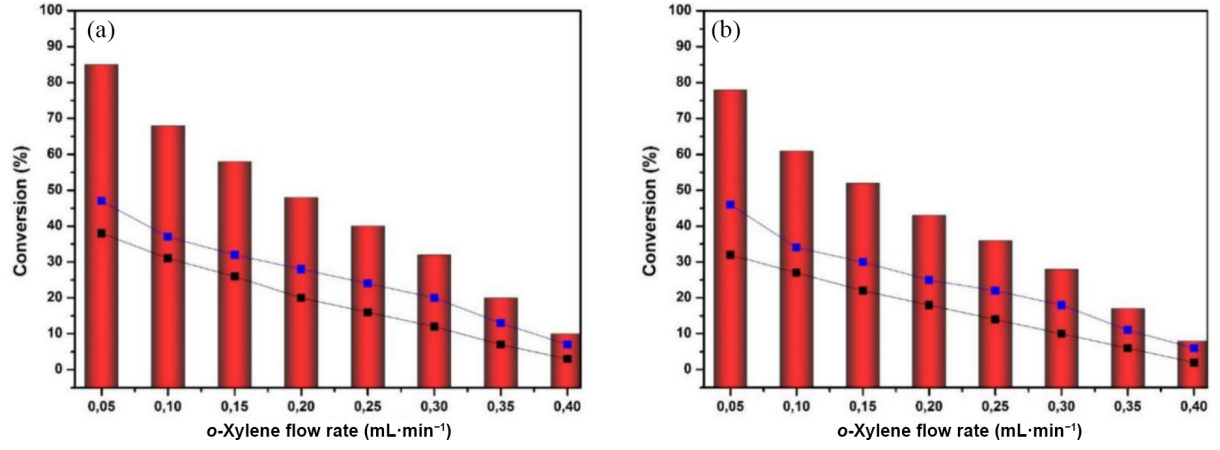

Figure 8 Hydroconversion of *o*-xylene to **1,2-DMCH** under varying substrate flow rates using (a) $\mathbf{Pt_3W_{11}}$**-SBA-15-apts** and (b) $\mathbf{Pt^{II}_2W_5}$**-SBA-15-apts** as catalysts. The curves represent the percentage of ***cis*-1,2-DMCH** (black) and ***trans*-1,2-DMCH** (blue) isomers in the product. Reaction conditions: 310 °C, 28 bar H_2.

reported by Kortz's group [69], which achieved 100% conversion under similar conditions, our results for **Pt_3W_{11}** suggest that while both systems share trinuclear platinum features, differences in ligand environment (S vs. O), counterions, and Pt-site accessibility, especially after calcination, have a significant impact on catalytic behavior [69, 70]. Mechanistically, hydrogenation likely proceeds via sequential H_2 activation on the Pt centers, followed by π-complexation and stepwise hydrogen addition to the aromatic ring, a pathway well-established for noble metal surfaces [71, 72]. The performance of **Pt_3W_{11}** underscores the importance of rational design of the POM framework, ensuring its thermal stability, maximizing Pt dispersion, and minimizing steric hindrance to optimize hydrogenation efficiency under continuous-flow conditions.

4 Conclusions

The three new platinum-containing isopolytungstates—$[Pt_3W_{11}O_{41}]^{64-}$ (**Pt_3W_{11}**), $[Pt^{II}_2W_5O_{18}((CH_3)_2AsO_2)_2]^{4-}$ (**$Pt^{II}_2W_5$**), and $[Pt^{III}_2W_5O_{18}((CH_3)_2AsO_2)_4]^{4-}$ (**$Pt^{III}_2W_5$**)—were synthesized in aqueous media and characterized via ^{1}H, ^{13}C, and ^{195}Pt NMR spectroscopy. The polyanion $[Pt_3W_{11}O_{41}]^{64-}$ consists of three $\{W_3O_{13}\}$ and one $\{W_2O_{10}\}$ fragments connected via three Pt atoms forming a linear $\{Pt_3O_{12}\}$ triad, which exhibits direct Pt–Pt bonding (2.64–2.68 Å). The distances between the Pt atoms and the oxygen atoms from the neighboring **Pt_3W_{11}** polyanions (Pt···O distances of 2.34 and 2.65 Å) suggest a [4+1] coordination for the outer platinum centers, indicating weak inter-polyanion interactions. XPS analysis of **Pt_3W_{11}** confirms the presence of a mixture of Pt^{IV} and Pt^{III} in a 1:4 ratio. DFT calculations suggest that **Pt_3W_{11}** comprises a mixture of $[Pt_3W_{11}\ 2e]^{6-}$ and $[Pt_3W_{11}\ 3e]^{7-}$ in a 3:2 ratio, which is significantly more stable than a combination of $[Pt_3W_{11}]^{4-}$ and $[Pt_3W_{11}\ 3e]^{7-}$ in a 1:4 ratio. A 3:1:1 mixture of $[Pt_3W_{11}\ 3e]^{7-}$, $[Pt_3W_{11}\ 2e]^{6-}$, and $[Pt_3W_{11}\ 1e]^{5-}$is also possible; however, it is slightly higher in energy than the 3:2 combination. These results indicate that the oxidation state of each Pt center within a **Pt_3W_{11}** polyanion cannot be neatly assigned as +3 or +4, suggesting a Robin–Day class III behavior within the Pt_3 moiety. In addition, formal covalent bonding between Pt atoms was confirmed through a topological analysis of the calculated electron density. The polyoxoanions **$Pt^{II}_2W_5$** and **$Pt^{III}_2W_5$** both consist of a monolacunary Lindqvist fragment, $\{W_5O_{18}\}^{6-}$, coordinated via either two Pt^{II} ions in a square-planar coordination geometry or two Pt^{III} ions in a square-pyramidal coordination geometry with direct Pt–Pt bonding (2.64 Å), respectively. These results demonstrate how the Pt oxidation state and coordination geometry influence the electronic structure of POMs, offering new design principles for catalytic or electronic materials. In addition to the structural characterization, the immobilized **Pt_3W_{11}** and **$Pt^{II}_2W_5$** ions on SBA-15-apts were evaluated as precatalysts for the continuous-flow hydrogenation of *o*-xylene under high-pressure hydrogen. Notably, during calcination and hydrogenation, the initial POMs are fully reduced, yielding metallic Pt(0) nanoparticles as the true catalyst. The supported **Pt_3W_{11}** showed superior performance, achieving 85% conversion at 310 °C, compared to 78% for **$Pt^{II}_2W_5$**, which is attributable to its higher platinum density and greater thermal robustness. A temperature-dependent shift in product selectivity from *cis*- to *trans*-1,2-dimethylcyclohexane was observed, reflecting a transition from kinetic to thermodynamic control. Flow rate variation studies at 310 °C further highlighted the significance of residence time in maximizing conversion. Both catalysts retained high activity and selectivity over five consecutive cycles, underscoring their structural and operational stability. These results underline the importance of rational POM design, oxidation-state control, and support functionalization in developing robust and efficient hydrogenation catalysts.

Electronic Supplementary Material: Supplementary material (preparation details, experimental and calculated structural data, electronic information on the Pt_3 system, details on the catalytic activity of several systems for o-xylene hydrogenation, thermograms and FTIR spectra of Pt_2 and Pt_3 systems) is available in the online version of this article at https://doi.org/10.26599/POM.2025.9140107.

Data availability

All data needed to support the conclusions in the paper are presented in the manuscript and the Electronic Supplementary Material. Additional data related to this paper may be requested from the corresponding author upon request.

CSD 2414132, CCDC 2414130, CCDC 2414131 contain the supplementary crystallographic data for this paper. These data can be obtained free of charge via www.ccdc.cam.ac.uk/structures/, or by emailing data_request@ccdc.cam.ac.uk, or by contacting The Cambridge Crystallographic Data Centre, 12 Union Road, Cambridge CB2 1EZ, UK; fax: +44 1223 336033.

Acknowledgements

U. K. thanks the German Research Council (DFG, KO-2288/26-1, KO-2288/29-1, KO-2288/31-1) and Constructor University for support. J. Y. Z. sincerely acknowledges China Scholarship Council (CSC) for a doctoral fellowship. X. L., K. M. and J. M. P. thank the Spanish Ministry of Science (grant PID2020-112762GB-I00 funded by MCIN/AEI/10.13039/501100011033) and the Generalitat de Catalunya (grant 2021 SGR 00110) for financial support.

Declaration of competing interest

There are no conflicts to declare. Author Ulrich Kortz is the editorial board member of this journal, but he is not involved in the peer-review or decision of this article.

Author contribution statement

J. Y. Z: Data curation, validation, writing manuscript. S. B.: Data curation, validation. M. E. M.: Data curation, validation, writing manuscript. T. N.: Data curation, validation, writing manuscript. K. M.: Data curation, writing manuscript. X. L.: Data curation, writing manuscript, experimental design, supervision. J. M. P.: Project administration, funding acquisition, supervision. V. W.: Experimental design, supervision. U. K.: Project administration, funding acquisition, supervision. All the authors have approved the final manuscript.

Use of AI statement

None.

References

[1] Pope, M. T. *Heteropoly and Isopoly Oxometalates*; Springer: Berlin,

Heidelberg, **1983**.
[2] Putaj, P.; Lefebvre, F. Polyoxometalates containing late transition and noble metal atoms. *Coord. Chem. Rev.* **2011**, *255*, 1642–1685.
[3] Izarova, N. V.; Pope, M. T.; Kortz, U. Noble metals in polyoxometalates. *Angew. Chem., Int. Ed.* **2012**, *51*, 9492–9510.
[4] Qian, D. Q.; Lin, Y. D.; Xiao, H. P.; Wu, B.; Li, X. X.; Zheng, S. T. Advances in coinage-metal-substituted polyoxometalates: A review. *Polyoxometalates* **2024**, *3*, 9140040.
[5] Pley, M.; Wickleder, M. S. The cluster ion $[Pt_{12}O_8(SO_4)_{12}]^{4-}$. *Angew. Chem., Int. Ed.* **2004**, *43*, 4168–4170.
[6] Yang, P.; Kortz, U. Discovery and evolution of polyoxopalladates. *Acc. Chem. Res.* **2018**, *51*, 1599–1608.
[7] Chubarova, E. V.; Dickman, M. H.; Keita, B.; Nadjo, L.; Miserque, F.; Mifsud, M.; Arends, I. W. C. E.; Kortz, U. Self-assembly of a heteropolyoxopalladate nanocube: $[Pd^{II}_{13}As^{V}_{8}O_{34}(OH)_6]^{8-}$. *Angew. Chem., Int. Ed.* **2008**, *47*, 9542–9546.
[8] Izarova, N. V.; Vankova, N.; Heine, T.; Biboum, R. N.; Keita, B.; Nadjo, L.; Kortz, U. Polyoxometalates made of gold: The polyoxoaurate $[Au^{III}_4As^{V}_4O_{20}]^{8-}$. *Angew. Chem., Int. Ed.* **2010**, *49*, 1886–1889.
[9] Zhang, J. Y.; Bhattacharya, S.; Khsara, B. E.; Nisar, T.; Müller, A. B.; Besora, M.; Poblet, J. M.; Wagner, V.; Kuhnert, N.; Kortz, U. Pt^{IV}-containing hexaplatinate(II) $[Pt^{IV}Pt^{II}_6O_6(AsO_2(CH_3)_2)_6]^{2-}$ and hexapalladate(II) $[Pt^{IV}Pd^{II}_6O_6(AsO_2(CH_3)_2)_6]^{2-}$. *Inorg. Chem.* **2023**, *62*, 13184–13194.
[10] Lee, U.; Kobayashi, A.; Sasaki, Y. Structure of pentasodium trihydrogenhexatungstoplatinate(IV) icosahydrate, $Na_5[H_3PtW_6O_{24}].20H_2O$. *Acta Cryst.* **1983**, *C39*, 817–819.
[11] Lee, U.; Sasaki, Y. Isomerism of the hexamolybdo-platinate(IV) polyanion. Crystal structures of $K_{3.5}[\alpha\text{-}H_{4.5}PtMo_6O_{24}]\cdot 3H_2O$ and $(NH_4)_4[\beta\text{-}H_4PtMo_6O_{24}]\cdot 1.5H_2O$. *Chem. Lett.* **1984**, *13*, 1297–1300.
[12] Lee, U.; Joo, H. C.; Park, K. M.; Mal, S. S.; Kortz, U.; Keita, B.; Nadjo, L. Facile incorporation of platinum(IV) into polyoxometalate frameworks: Preparation of $[H_2Pt^{IV}V_9O_{28}]^{5-}$ and characterization by ^{195}Pt NMR Spectroscopy. *Angew. Chem., Int. Ed.* **2008**, *47*, 793–796.
[13] Abramov, P. A.; Vicent, C.; Kompankov, N. B.; Gushchin, A. L.; Sokolov, M. N. Platinum polyoxoniobates. *Chem. Commun.* **2015**, *51*, 4021–4023.
[14] Kuznetsova, A. A.; Volchek, V. V.; Yanshole, V. V.; Fedorenko, A. D.; Kompankov, N. B.; Kokovkin, V. V.; Gushchin, A. L.; Abramov, P. A.; Sokolov, M. N. Coordination of Pt(IV) by $\{P_8W_{48}\}$ macrocyclic inorganic cavitand: Structural, solution, and electrochemical studies. *Inorg. Chem.* **2022**, *61*, 14560–14567.
[15] Sokolov, M. N.; Adonin, S. A.; Peresypkina, E. V.; Fedin, V. P. A Pt(II) isopolytungstate: Synthesis and crystal structure. *Dalton Trans.* **2012**, *41*, 11978–11979.
[16] Kato, M.; Kato, C. N. A Keggin-type polyoxotungstate-coordinated diplatinum(II) complex: Synthesis, characterization, and stability of the *cis*-platinum(II) moieties in dimethylsulfoxide and water. *Inorg. Chem. Commun.* **2011**, *14*, 982–985.
[17] Kato, C. N.; Morii, Y.; Hattori, S.; Nakayama, R.; Makino, Y.; Uno, H. Diplatinum(II)-coordinated polyoxotungstate: Synthesis, molecular structure, and photocatalytic performance for hydrogen evolution from water under visible-light irradiation. *Dalton Trans.* **2012**, *41*, 10021–10027.
[18] Deng, W. P.; Zhang, Q. H.; Wang, Y. Polyoxometalates as efficient catalysts for transformations of cellulose into platform chemicals. *Dalton Trans.* **2012**, *41*, 9817–9831.
[19] Lin, Z. G.; Izarova, N. V.; Kondinski, A.; Xing, X. L.; Haider, A.; Fan, L. Y.; Vankova, N.; Heine, T.; Keita, B.; Cao, J. et al. Platinum-containing polyoxometalates: *Syn*-and *anti*-$[Pt^{II}_2(\alpha\text{-}PW_{11}O_{39})_2]^{10-}$ and formation of the metal-metal-bonded di-Pt^{III} derivatives. *Chem.—Eur. J.* **2016**, *22*, 5514–5519.
[20] Kato, C. N.; Nagatani, S.; Mizuno, T. Synthesis, characterization, and stability of α-keggin-type polyoxotungstate-coordinated mono-platinum(II) complex. *Eur. J. Inorg. Chem.* **2019**, *2019*, 517–522.
[21] Yu, F. Y.; Lang, Z. L.; Yin, L. Y.; Feng, K.; Xia, Y. J.; Tan, H. Q.; Zhu, H. T.; Zhong, J.; Kang, Z. H.; Li, Y. G. Pt–O bond as an active site superior to Pt^0 in hydrogen evolution reaction. *Nat. Commun.* **2020**, *11*, 490.
[22] Yu, F. Y.; Lang, Z. L.; Zhou, Y. J.; Feng, K.; Tan, H. Q.; Zhong, J.; Lee, S. T.; Kang, Z. H.; Li, Y. G. Revealing hydrogen evolution performance of single-atom platinum electrocatalyst with polyoxometalate molecular models. *ACS Energy Lett.* **2021**, *6*, 4055–4062.
[23] Albano, V. G.; Natile, G.; Panunzi, A. Five-coordinate alkene complexes of palladium(II) and platinum(II). *Coord. Chem. Rev.* **1994**, *133*, 67–114.
[24] Annunziata, A.; Cucciolito, M. E.; Esposito, R.; Ferraro, G.; Monti, D. M.; Merlino, A.; Ruffo, F. Five-coordinate platinum(II) compounds as potential anticancer agents. *Eur. J. Inorg. Chem.* **2020**, *2020*, 918–929.
[25] Fanizzi, F. P.; Intini, F. P.; Maresca, L.; Natile, G.; Lanfranchi, M.; Tiripicchio, A. Four-*versus* five-co-ordination in palladium(II) and platinum(II) complexes containing 2,9-dimethyl-1,10-phenanthroline (dmphen). Crystal structures of $[PtCl_2(dmphen)]$ and $[Pt(\eta^2\text{-}C_2H_4)Cl_2(dmphen)]$. *J. Chem. Soc., Dalton Trans.* **1991**, 1007–1015.
[26] Benedetti, M.; Lamacchia, V.; Antonucci, D.; Papadia, P.; Pacifico, C.; Natile, G.; Fanizzi, F. P. Insertion of alkynes into Pt-X bonds of square planar $[PtX_2(N\text{^}N)]$ (X = Cl, Br, I) complexes. *Dalton Trans.* **2014**, *43*, 8826–8834.
[27] Albano, V. G.; Monari, M.; Orabona, I.; Panunzi, A.; Ruffo, F. Oxidative additions of E–E bonds (E = Chalcogen) to group 10 metals: "Tunable" cleavage of Se–Se bonds by Pt(0) complexes. *J. Am. Chem. Soc.* **2001**, *123*, 4352–4353.
[28] Albano, V. G.; Monari, M.; Orabona, I.; Panunzi, A.; Roviello, G.; Ruffo, F. Synthesis and characterization of trigonal-bipyramidal platinum(II) olefin complexes with chalcogenide ligands in axial positions. X-ray molecular structures of $[Pt(SMe)_2(dmphen)(diphenyl\ fumarate)]$, its cationic dipositive derivative $[Pt(SMe_2)_2(dmphen)(diphenyl\ fumarate)][BF_4]_2$, and free diphenyl fumarate. *Organometallics* **2003**, *22*, 1223–1230.
[29] Albano, V. G.; Castellari, C.; Ferrara, M. L.; Panunzi, A.; Ruffo, F. Five-coordinate hydrido-complexes $[PtX(H)(N,N\text{-chelate})(olefin)]$ (X = Cl, Br or I). Crystal structure of $[PtCl(H)(2,9\text{-}Me_2\text{-}1,10\text{-}phenanthroline)(dimethyl\ maleate)]$. *J. Organomet. Chem.* **1994**, *469*, 237–244.
[30] De Felice, V.; De Renzi, A.; Ruffo, F.; Tesauro, D. Three-coordinate Pt(O) η^2-complexes: Electrophilic hydrogen attack through oxidative-addition of protic acids. *Inorg. Chim. Acta* **1994**, *219*, 169–178.
[31] Albano, V. G.; Braga, D.; De Felice, V.; Panunzi, A.; Vitagliano, A. Five-coordinate olefin complexes of platinum(II) containing σ-bonded carbon ligands. Synthesis and characterization of $[PtClMe(\eta^2\text{-}C_2H_4)(N\text{–}N')]$ complexes. Molecular structure of an adduct with a chiral metal center and of its parent four-coordinate complex. *Organometallics* **1987**, *6*, 517–525.
[32] Cucciolito, M. E.; De Felice, V.; Panunzi, A.; Vitagliano, A. Five-coordinate olefin complexes of platinum(II) containing σ-bonded carbon ligands. Coordination environment and stability. *Organometallics* **1989**, *8*, 1180–1187.
[33] Ferrara, M. L.; Orabona, I.; Ruffo, F.; De Felice, V. Coordinatively saturated olefin platinum(II) complexes containing two η^1-C-bonded groups. *J. Organomet. Chem.* **1996**, *519*, 75–82.
[34] Cucciolito, M. E.; Panunzi, A.; Ruffo, F.; Albano, V. G.; Monari, M. First coordinatively saturated carbene complexes of platinum(II): Synthesis, structure, and reactivity. *Organometallics* **1999**, *18*, 3482–3489.
[35] Albano, V. G.; Castellari, C.; De Felice, V.; Panunzi, A.; Ruffo, F. Synthesis and characterization of five-coordinate platinum(II) complexes [Pt(2,9-dimethyl-1,10-phenanthroline) $(SnR_nX_{3-n})X$

(olefin)] (X). *J. Organomet. Chem.* **1992**, *425*, 177–188.
[36] Albano, V. G.; Castellari, C.; Monari, M.; De Felice, V.; Ferrara, M. L.; Ruffo, F. Organolead derivatives of coordinatively saturated platinum(II) olefin complexes. Molecular structure of [PtCl(PbPh2Cl)(2,9-dimethyl-1,10-phenanthroline)(dimethyl maleate)] and its deplumbation product [PtCl(Ph)(2,9-dimethyl-1,10-phenanthroline)(dimethyl maleate)]. *Organometallics* **1995**, *14*, 4213–4221.
[37] Albano, V. G.; Castellari, C.; Monari, M.; De Felice, V.; Panunzi, A.; Ruffo, F. Addition-elimination equilibria involving 16e⁻ platinum(0) and 18e⁻ platinum(II) complexes. *Organometallics* **1996**, *15*, 4012–4019.
[38] Albano, V. G.; Ferrara, M. L.; Monari, M.; Panunzi, A.; Ruffo, F. Synthesis of five-coordinate Pt(II) complexes containing organogermanium fragments in axial position: Structure of [PtCl($GePh_2$Cl)(2,9-Me_2-1,10-phen)(CH_2CH_2)]. *Inorg. Chim. Acta* **1999**, *285*, 70–75.
[39] Sanchez, A.; Castellari, C.; Panunzi, A.; Vitagliano, A.; De Felice, V. New cationic five-coordinate monoolefin hydrocarbyl complexes of platinum(II). *J. Organomet. Chem.* **1990**, *388*, 243–252.
[40] Albano, V. G.; Castellari, C.; Monari, M.; De Felice, V.; Panunzi, A.; Ruffo, F. Synthesis and characterization of five-coordinate platinum [PtCl(L)(N-N)(olefin)]$^+$ complexes. Molecular structure of [PtCl(pyridine)(2,9-dimethyl-1,10-phenanthroline)(ethylene)](CF_3SO_3). *Organometallics* **1992**, *11*, 3665–3669.
[41] Calvanese, L.; Cucciolito, M. E.; D'Amora, A.; D'Auria, G.; Esposito, A.; Esposito, R.; Falcigno, L.; Ruffo, F. Recognition of prochiral sulfides in five-coordinate Pt^{II} complexes. *Eur. J. Inorg. Chem.* **2015**, *2015*, 4068–4075.
[42] *CrysAlis^{Pro} Software system*, version 1.171.38.46, *Rigaku Oxford Diffraction*; Rigaku Corporation: Oxford, UK, **2017**.
[43] *ABSPACK, SCALE*. "*Empirical absorption correction*." *CrysAlis^{Pro}-Software Package, Rigaku Oxford Diffraction*; Rigaku Corporation: Oxford, UK, **2022**.
[44] *SAINT*, Version 7.56a and *SADABS*, Version 2008/1; Bruker AXS Inc., Madison, Wisconsin, USA, **2008**.
[45] Sheldrick, G. M. *Program for Crystal Structure Refinement*; University of Göttingen: Göttingen, Germany, **2014**.
[46] Spek, A. L. *PLATON, a multipurpose crystallographic tool*; Utrecht University: Utrecht, The Netherlands, **2002**.
[47] Blackwood, J. E.; Blower, R. E. Jr.; Layten, S. W.; Lillie, D. H.; Lipkus, A. H.; Peer, J. P.; Qian, C.; Staggenborg, L. M.; Watson, C. E. Chemical abstracts service chemical registry system. 13. Enhanced handling of stereochemistry. *J. Chem. Inf. Comput. Sci* **1991**, *31*, 204–212.
[48] Romerosa, A.; Suarez-Varela, J.; Hidalgo, M. A.; Avila-Rosón, J. C.; Colacio, E. Synthesis and molecular structure of the first metal complex of an analogue of guanine with Pd^{II}–C(8) binding. *Inorg. Chem.* **1997**, *36*, 3784–3786.
[49] Quintal, S. M. O.; Nogueira, H. I. S.; Félix, V.; Drew, M. G. B. Coordination modes of 3-hydroxypicolinic acid: Synthesis and crystal structures of palladium(II), platinum(II) and rhenium(V) complexes. *New J. Chem.* **2000**, *24*, 511–517.
[50] Frisch, M. J.; Trucks, G. W.; Schlegel, H. B.; Scuseria, G. E.; Robb, M. A.; Cheeseman, J. R.; Scalmani, G.; Barone, V.; Petersson, G. A.; Nakatsuji, H. et al. *Gaussian 09*, Revision C.01; Gaussian, Inc.: Wallingford, CT, USA, **2016**.
[51] Chiodo, S.; Russo, N.; Sicilia, E. LANL2DZ basis sets recontracted in the framework of density functional theory. *J. Chem. Phys.* **2006**, *125*, 104107.
[52] Ernzerhof, M.; Scuseria, G. E. Assessment of the Perdew-Burke-Ernzerhof exchange-correlation functional. *J. Chem. Phys.* **1999**, *110*, 5029–5036.
[53] Grimme, S.; Ehrlich, S.; Goerigk, L. Effect of the damping function in dispersion corrected density functional theory. *J. Comput. Chem.* **2011**, *32*, 1456–1465.
[54] Miertuš, S.; Scrocco, E.; Tomasi, J. Electrostatic interaction of a solute with a continuum. A direct utilizaion of AB initio molecular potentials for the prevision of solvent effects. *Chem. Phys.* **1981**, *55*, 117–129.
[55] Kondinski, A. Metal-metal bonds in polyoxometalate chemistry. *Nanoscale* **2021**, *13*, 13574–13592.
[56] Bader, R. F. W. *Atoms in Molecules: A Quantum Theory*; Oxford University Press: Oxford, **1990**.
[57] Lepetit, C.; Fau, P.; Fajerwerg, K.; Kahn, M. L.; Silvi, B. Topological analysis of the metal-metal bond: A tutorial review. *Coord. Chem. Rev.* **2017**, *345*, 150–181.
[58] Lim, B. S.; Rahtu, A.; Park, J. S.; Gordon, R. G. Synthesis and characterization of volatile, thermally stable, reactive transition metal amidinates. *Inorg. Chem.* **2003**, *42*, 7951–7958.
[59] Cotton, F. A.; Walton, R. A. *Multiple Bonds Between Metal Atoms*; Wiley: New York, **1982**.
[60] Wei, X. Y.; Dickman, M. H.; Pope, M. T. New routes for multiple derivatization of polyoxometalates. Bis(acetato)dirhodium-11-tungstophosphate, $[(PO_4)W_{11}O_{35}\{Rh_2(OAc)_2\}]^{5-}$. *Inorg. Chem.* **1997**, *36*, 130–131.
[61] Pley, M.; Wickleder, M. S. $Pt_2(HSO_4)_2(SO_4)_2$, the first binary sulfate of platinum. *Z. Anorg. Allg. Chem.* **2004**, *630*, 1036–1039.
[62] Sokolov, M. N.; Korenev, V. S.; Peresypkina, E. V.; Fedin, V. P. Synthesis and crystal structure of $Cs_7[BW_{12}O_{40}][Rh_2(CH_3COO)_4Cl]_2 \cdot 8H_2O$. *Russ. J. Coord. Chem.* **2011**, *37*, 133–136.
[63] Cherkashina, N. V.; Nefedov, S. E.; Klyagina, A. P.; Markov, A. A.; Vargaftik, M. N.; Moiseev, I. I. The first molecular paddlewheel platinum(III) acetate complex $Pt_2(\mu\text{-}OOCMe)_4(O_3SMe)_2$. *Inorg. Chem. Commun.* **2012**, *21*, 39–42.
[64] Still, B. M.; Kumar, P. G. A.; Aldrich-Wright, J. R.; Price, W. S. ^{195}Pt NMR—Theory and application. *Chem. Soc. Rev.* **2007**, *36*, 665–686.
[65] Klonowski, P.; Goloboy, J. C.; Uribe-Romo, F. J.; Sun, F. R.; Zhu, L. Y.; Gándara, F.; Wills, C.; Errington, R. J.; Yaghi, O. M.; Klemperer, W. G. Synthesis and characterization of the platinum-substituted Keggin anion $\alpha\text{-}H_2SiPtW_{11}O_{40}^{4-}$. *Inorg. Chem.* **2014**, *53*, 13239–13246.
[66] Kuznetsova, N. I.; Detusheva, L. G.; Kuznetsova, L. I.; Fedotov, M. A.; Likholobov, V. A. Complexes of palladium(II) and platinum(II) with the $PW_{11}O_{39}^{7-}$ heteropolyanion as catalytically active species in benzene oxidation. *J. Mol. Catal. A: Chem.* **1996**, *114*, 131–139.
[67] Legagneux, N.; Jeanneau, E.; Thomas, A.; Taoufik, M.; Baudouin, A.; de Mallmann, A.; Basset, J. M.; Lefebvre, F. Grafting reaction of platinum organometallic complexes on silica-supported or unsupported heteropolyacids. *Organometallics* **2011**, *30*, 1783–1793.
[68] Dugar, S.; Izarova, N. V.; Mal, S. S.; Fu, R. Q.; Joo, H. C.; Lee, U.; Dalal, N. S.; Pope, M. T.; Jameson, G. B.; Kortz, U. Characterization of Pt^{IV}-containing polyoxometalates by high-resolution solid-state ^{195}Pt and ^{51}V NMR spectroscopy. *New J. Chem.* **2016**, *40*, 923–927.
[69] Rajan, A.; Elcheikh Mahmoud, M.; Wang, F.; Bhattacharya, S.; Mougharbel, A. S.; Ma, X.; Müller, A. B.; Nisar, T.; Taffa, D. H.; Poblet, J. M. et al. Discovery of polythioplatinate(II) $[Pt_3S_2(SO_3)_6]^{10-}$ and study of its solution and catalytic properties. *Inorg. Chem.* **2022**, *61*, 11529–11538.
[70] Ayass, W. W.; Miñambres, J. F.; Yang, P.; Ma, T.; Lin, Z. G.; Meyer, R.; Jaensch, H.; Bons, A. J.; Kortz, U. Discrete polyoxopalladates as molecular precursors for supported palladium metal nanoparticles as hydrogenation catalysts. *Inorg. Chem.* **2019**, *58*, 5576–5582.
[71] Rylander, P. N. *Hydrogenation Methods*; Academic Press: London, **1985**.
[72] Wu, S.; Zhao, C. C.; Dong, Y. J.; Yan, L. K. Cyclohexanone hydrogenation to cyclohexanol on phosphomolybdate supported Pt single-atom catalyst: A density functional theory study. *Polyoxometalates* **2024**, *3*, 9140070.

Jiayao Zhang obtained a PhD in 2023 at Constructor University (formerly Jacobs University) in Bremen, Germany under the supervision of Prof. Ulrich Kortz. Her research focuses on the synthesis, characterization and application of polyoxo-noble-metalates.

Saurav Bhattacharya is Assistant Professor in the Department of Chemistry of BITS Pilani K. K. Birla Goa campus since 2022. Before doing so, he obtained his PhD from the Indian Institute of Science Bangalore (2009-2016) and subsequently worked as a postdoctoral researcher at Constructor University (formerly Jacobs University) in Bremen, Germany (2016-2022). His research interests primarily lie in the area of synthesis and structural determination of transition metal- and noble metal-oxo clusters integrated into Metal-Organic Frameworks (MOFs) and study their efficacy as heterogeneous catalysts in important organic coupling reactions as well as oxidative and reductive transformations that yield important value-added products.

Mahmoud Elcheikh Mahmoud is a Ph.D. student at Constructor University under the supervision of Prof. Ulrich Kortz. His research focuses on the synthesis and characterization of 3d- and f-block metal-based polyoxotungstates, as well as their application in catalysis, including hydrogenation and oxidation reactions.

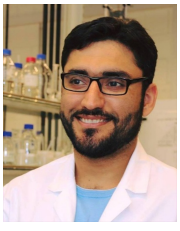

Talha Nisar received a Ph.D. in Physics in 2021 from Jacobs University Bremen (now Constructor University). He is currently a postdoctoral researcher at the Institute for Applied Materials (IAM), Karlsruhe Institute of Technology (KIT), and a guest scientist at Constructor University. His research focuses on thin-film growth using solution-based techniques and atomic layer deposition (ALD), with applications in device physics and catalysis.

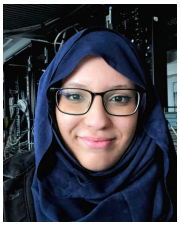

Khaoula Merimi is a Ph.D. student at Universitat Rovira i Virgili under the supervision of Prof. Xavier López. Her research focuses on the computational study of molecular and surface-deposited polyoxometalates, with emphasis on electronic structure, NMR properties, and molecular dynamics simulations.

Xavier López is a professor at Universitat Rovira i Virgili, where he received his Ph.D. in 2003. His research mainly focuses on the electronic structure and solution behavior of polyoxometalates, and on the electronic excited states and associated energy-transfer processes in organic chromophores.

Josep M. Poblet is Emeritus Professor of Physical Chemistry at the Universitat Rovira i Virgili (URV). He received his PhD from the University of Barcelona in 1983 and has developed most of his academic career at URV, where he obtained a full professorship in 2001. He served as Director of the Department of Physical and Inorganic Chemistry for approximately 12 years and has received several awards.

Veit Wagner is a Physics professor at Constructor University (formerly Jacobs University) in Bremen, Germany since 2002. He received a Ph.D. in Physics in 1995 at TU Berlin and RWTH Aachen, followed by a postdoctoral research stay at University Notre-Dame de la Paix in Namur, Belgium. His research interests lie in the areas of molecular and nanoelectronics, hybrid organic systems, organic surfaces and interfaces.

Ulrich Kortz is a Chemistry professor at Constructor University (formerly Jacobs University) in Bremen, Germany since 2002. He obtained a Ph.D. at Georgetown University in Washington, DC under the supervision of M. T. Pope (1995), followed by postdoctoral research stays at the University of Florence, Italy (D. Gatteschi) and the University of Versailles, France (G. Hervé, A. Tézé). In 1997 he started his independent academic career at the American University of Beirut (AUB) in Lebanon. His research interests include synthetic inorganic and organometallic chemistry, structural chemistry, polyoxometalates, polyoxo-noble-metalates, MOFs, catalysis, magnetism, and electrochemistry.